Metallic quantum dots

2005 J. Phys.: Condens. Matter 17 S1075

(http://iopscience.iop.org/0953-8984/17/13/004)

INSTITUTE OF PHYSICS PUBLISHING JOURNAL OF PHYSICS: CONDENSED MATTER

J. Phys.: Condens. Matter **17** (2005) S1075–S1094 doi:10.1088/0953-8984/17/13/004

Metallic quantum dots

V Lindberg[1] **and B Hellsing**[2]

[1] Department of Physics, Växjö University, SE-351 95 Växjö, Sweden
[2] Department of Physics, Göteborg University, SE-412 96 Göteborg, Sweden

E-mail: vanja.lindberg@msi.vxu.se

Received 31 December 2004
Published 18 March 2005
Online at stacks.iop.org/JPhysCM/17/S1075

Abstract

In a quantum dot, the electrons are confined in all three dimensions to a length scale of the order of the electron Fermi wavelength. Due to the confinement, quantum effects will dominate over the bulk properties and the energy spectrum becomes discrete, similar to that of an atom. In this review, we present a short introduction to electron confinement in nanosize structures and properties related to quantum size effects. Furthermore, we present a model for calculation of the electronic structure of adsorbed quantum dots, where we have focused on the system of Na on Cu(111). Our results are compared to experimental results from scanning tunnelling microscopy and photoemission spectroscopy. In addition, we present a study of CO adsorption on a small Na quantum dot. The resulting charge transfer turns out to depend critically on the size of the quantum dot, and the results are discussed in terms of electron structure and symmetry of relevant electron orbitals.

1. Introduction

Today, nanoscience presents a very active research area, bringing together researchers from many areas like physics, chemistry, materials science, electronics, biology and medicine. The emphasis is on trying to understand the relationship between the structure of the material and its optical, chemical and electronic properties, but also to develop and improve techniques for manufacturing nanomaterials for new applications. Nanomaterials show large industrial potential, with applications in areas such as new electronic components, detectors, lasers, smart materials and catalysts.

When the dimensions are minimized to a scale of the order of the Fermi wavelength of the electron, the behaviour will be dominated by the rules of quantum mechanics [1, 2], and new properties will develop that may be totally different from the bulk properties, and sometimes completely unexpected. One well-known example is provided by gold, which changes in both physical and chemical character when dispersed as nanoparticles. Bulk gold has a yellowish colour, while nanoparticulate gold gives a ruby-red, purple or even blue colour, depending on

the nanoparticle size [3, 4]. In addition, the catalytic activity is changed when the nanoparticle regime is reached. Gold is a noble metal, and in its bulk form quite inert, but oxide supported gold clusters have shown very high chemical activity [5, 6, 8, 7], and have proved to be very well suited for use as chemical catalysts [9].

About ten years ago, Crommie and co-workers [1] presented a method for confining electrons to artificial structures on the nanometre scale, referred to as *quantum corrals*. These synthetic structures were formed by deliberately assembling Fe adatoms to enclosed structures on a Cu(111) surface by using the tip of a scanning tunnelling microscope (STM). The experiment was performed at ultrahigh vacuum and extremely low temperature. The surface electrons become confined laterally to the adatom structure because of the strong scattering that occurs at the Fe atoms [1], and perpendicular to the surface due to the bandgap that exists for the (111) face of noble metals [10]. The spectroscopic results showed very nice agreement with theoretical values for a corresponding two-dimensional (2D) circular potential well with hard walls, and by recording the local density of states (LDOS) at low bias voltage with the STM, it was possible to observe directly the standing wave patterns of the confined electron states. The nodal pattern could be accounted for by a linear combination of the electron density corresponding to the states close to E_F, as calculated from a 2D model. Another nice example is provided by the stadium shaped quantum corral [11, 12].

A natural way of forming low dimensional structures on metal surfaces is by controlled growth of epitaxial layers [2]. With an appropriate choice of deposition and annealing temperatures small islands of different sizes and symmetries, so-called quantum dots (QD), may form [13]. The QDs arise when it is energetically more favourable for the film to relax by forming islands than to form dislocations [10]. As an example, close packed surfaces of noble metals have proved suitable as a basis for 2D island growth. Ag islands one monolayer (ML) high are formed naturally during epitaxial growth on Ag(111) at room temperature [2, 14, 15], and also the second ML of Na on Cu(111) grows via island formation [16–20]. Individual atomic events can strongly influence or even dominate the microstructure and nanostructure of epitaxial films [21, 22]. The exact morphology of the surface depends critically on the interaction of the adatoms with the substrate as well as the growth process itself, including evaporation rates [23, 24], temperature [25, 26], pressure [27], post-annealing [28], dislocations [29] and substrate impurities [30, 31]. By creating surfaces with a periodic strain-relief pattern, ordered arrays of equally spaced monodispersed islands can be formed by atom diffusion and deposition [32, 33].

The self-assembled QDs have the advantage, in comparison with the quantum corrals, of being relatively stable even at room temperature [2] and at high voltages [14, 15]. This enables imaging for a wide range of voltages, without inducing structural damage. The STM [34, 35] presents an essential experimental tool for characterization of real space structure and electronic properties of adsorbed surface structures and defects [36, 37]. It has also proved useful for atomic level resolution of chemical surface reactions [32, 38, 39], and lately also lifetime studies of electronic states [40].

One important application for self-assembled quantum dots is in the field of catalysis. For large clusters, containing hundreds or thousands of electrons, the electronic properties are essentially those of the bulk and the resulting reactivity is due to surface electronic structure features and morphology effects like the density of kinks, steps and defects [41]. For small clusters on the other hand, with sizes that corresponds to the Fermi wavelength of the electron, the valence electrons are highly confined and quantum effects become dominant [1, 2, 42]. It has been observed that supported clusters often show a higher activity towards certain reaction than the corresponding bulk material and that the activity depends critically on the cluster size [8, 42, 44–46].

One very nice example is provided by gold, which is a noble metal and as a bulk material quite inert [3, 8, 46], but when dispersed as ultrafine particles on various metal oxides [5–7, 46, 47] as well as nanosized islands on titania oxide [8, 47, 48], gold exhibits extra high activity in many reactions like combustion of hydrocarbons [49], reduction of nitrogen oxide [50], propylene epoxidation [51] and in particular low temperature oxidation of carbon monoxide [5–8, 42, 43, 45–48]. For CO oxidation, the activity has been observed to depend critically on the nanoparticle size, the nature of the support as well as the detailed synthetic procedure [3, 47, 48]. STM results, reported by Valden *et al* [8, 45], showed that the reactivity to CO oxidation on TiO_2 supported 2D Au islands was size dependent with respect to the island height. The result was interpreted as a quantum size effect [8, 45]. Other experimental investigations emphasize coordination [52, 53], shape [54] and interface [55] effects. The activity of nanoparticulated gold has also attracted a lot of theoretical interest. First-principles calculations show a clear correlation between particle size and chemical activity, explained in terms of enhanced density of low coordination sites with decreasing cluster size [56, 57]. In addition the nature of the support plays an important role. Recent results [46, 58–60] show that the oxide provides excess charge to the Au cluster, which is important for the ability to bind and activate O_2. The gold–oxide support interface provides the most reactive sites [58], where the precise interface structure depends on the cluster size and geometry.

In this paper, we focus on self-assembled metallic QDs with emphasis on the system of Na on Cu(111), where the second ML of Na is grown via formation of approximately hexagonal 1 ML thick islands [16–20]. We present a model for calculating the electronic structure for this system [61, 62], and make comparisons to experimental results from STM and photoemission spectroscopy (PES). In addition, we study the size dependence of the reactivity for 1 ML thick Na quantum dots [63]. We show that the resulting charge transfer, between the approaching molecule and the QD, can be understood in terms of the electronic structure and symmetry which makes it possible to tune the charge transfer by changing the size parameters of the QD.

2. Na/Cu(111)

Close packed (111) surfaces of noble metals have a local bandgap perpendicular to the surface. When alkali metals are adsorbed on these surfaces, they form hexagonal structures at saturated ML coverage, following approximately the underlying structure [64]. The valence electrons of the alkali metal are confined to the surface by the vacuum barrier on one side and the local bandgap of the substrate on the other side, and form a 2D nearly free electron gas [65, 66]. The overlayer electron states show quantization properties similar to those of electrons confined to a one dimensional (1D) potential well [67], and are often referred to as *quantum well states* (QWS). The wavefunctions decay rapidly on the vacuum side, and have an oscillating tail decaying more slowly into the substrate [16], which can accommodate a substantial amount of electron charge. When Na is adsorbed on Cu(111), the first ML saturates at a coverage of $\Theta = 4/9$ [64, 68], corresponding to four Na atoms per nine surface Cu atoms yielding a $(3/2 \times 3/2)$ structure with a nearest neighbour distance of 7.43 au (1 au = 0.529 Å). The corresponding value for bulk Na is 6.92 au. If the Na deposition is continued, a second ML will start to grow. Results from PES [16, 17] indicated that the second ML grows via formation of 1 ML high islands. This was indeed verified by STM experiments [18–20]. Kliewer and co-workers [18] observed small 1 ML high Na islands already at a coverage of 1.1 ML.

The clean Cu(111) surface has a Shockley surface state within the bandgap at about 0.4 eV below the Fermi energy [69] at the $\bar{\Gamma}$ point of the surface Brillouin zone, corresponding to the binding energy in normal PES. The state exhibits a parabolic dispersion [70] characteristic for free electron-like surface states. When Na is deposited on the surface, the energy of the Cu

surface state decreases with increasing Na coverage [66, 71], and for coverage above $\Theta \approx 0.11$ the state is shifted below the band edge of the local bandgap [72] and is no longer visible in PES experiments. As the Na is deposited, Na-induced states will appear within the local bandgap. The lowest of these is a p-type QWS with one node in the direction perpendicular to the surface. It has a parabolic dispersion consistent with a free electron-like state [17, 71], and the energy decreases with increasing coverage. At a saturated ML coverage, it is situated at 0.1 eV below E_F [16, 17, 71]. In addition there are also unoccupied Na-induced states situated above the Fermi level, which have been observed and characterized by inverse photoelectron spectroscopy (IPES) [73] and two-photon photoemission (2PPE) [71]. During the growth of the second ML a new peak appears in the photoemission spectra for coverage above 1.3 ML at 0.1 eV above the Fermi level [16, 17]. This peak is ascribed to the 2 ML thick parts, and the position is shifted to somewhat lower energy as the coverage is increased. This shift in energy was ascribed to lateral quantum size effects as the Na islands grow larger [17].

The system of Na/Cu(111) has also attracted theoretical interest. A first-principles calculation [74] was performed to verify the existence of the QWS observed by PES. In addition, a first-principles study of the phonon-induced decay of a QWS hole was presented [75]. Here, we present results regarding electron structure and reactivity of the second-ML Na quantum dots. The electron structure has been calculated by using a three-dimensional finite potential well model [61] and by developing a two-density jellium model [62].

3. Computational method

Sodium is an alkali metal. Thus, the valence electrons are only weakly bound to the ions, forming a nearly free electron gas. When a Na quantum dot is formed on Cu(111), the valence electrons will be confined to the overlayer by the vacuum barrier on one side and the substrate bandgap on the other side. Since the confinement at the substrate side is not so very different from the vacuum barrier [65], a finite potential well model, section 3.1, could serve quite well as a first approximation. In order to get a more accurate description of the decay of the overlayer states into the substrate, we introduce a two-jellium model in section 3.2.

From STM experiments [18–20], we know that the second ML Na islands on Cu(111) are approximately hexagonal in shape. However, to simplify our calculations, we assume cylindrical symmetry. We do not believe that this will have a large effect on the general features.

3.1. Finite potential well model

We model the valence electrons confined within the QD by a finite potential barrier assuming cylindrical symmetry,

$$V(r, z, \psi) = \begin{cases} O & r < a \text{ and } -\frac{L}{2} < z < \frac{L}{2} \\ U_0 & \text{elsewhere,} \end{cases} \tag{1}$$

where U_0 is the constant potential barrier, a is the QD radius and L is the effective height. The Schrödinger equation is solved in cylindrical coordinates using atomic units ($e = m = \hbar = 1$),

$$(-\tfrac{1}{2}\nabla^2 + V(r, z, \phi))\Psi(r, z, \phi) = E\Psi(r, z, \phi). \tag{2}$$

Here, $\Psi(r, z, \phi)$ is the one-electron wavefunction, and E is the corresponding eigenenergy in atomic units (1 au = 27.2 eV). We denote the principal quantum number, referring to the quantization in the z-direction, by n and the azimuthal quantum number, implied by the axial

symmetry, by m. The l quantum number orders the orthogonal solutions with the same n and m.

The Schrödinger equation (2) is separated and solved semi-analytically, matching the analytic solutions for the interior and the exterior numerically at the boundary by requiring the wavefunction and its derivative to be continuous. The solutions for the internal ($r < a$) and external ($r > a$) regions are given by

$$\Psi^{<}_{nml}(r, z, \psi) = A_{nml}\Phi_n(z)J_m(k_{ml}r)\mathrm{e}^{\mathrm{i}m\phi} \tag{3a}$$

$$\Psi^{>}_{nml}(r, z, \psi) = B_{nml}\Phi_n(z)K_m(q_{ml}r)\mathrm{e}^{\mathrm{i}m\phi} \tag{3b}$$

where $q_{ml} = (2U_0 - k^2_{ml})^{1/2}$, A_{nml} and B_{nml} are normalization constants, $\Phi_n(z)$ are the wavefunctions corresponding to the quantization in the z-direction, and $J_m(k_{ml}r)$ and $K_m(q_{ml}r)$ are Bessel functions of the first and second kind respectively, corresponding to the radial solutions. The axial symmetry implies the angular solution $\mathrm{e}^{\mathrm{i}m\phi}$. The eigenenergies for (2) are given by

$$E_{nml} = \epsilon_n + \varepsilon_{ml}, \tag{4}$$

where ϵ_n is the eigenenergy achieved by solving the z part, and ε_{ml} corresponds to the lateral part. The parameters U_0 and L in (1) define the potential. Their values have been chosen by fitting the $\bar{\Gamma}$ point energy for the two lowest states with quantum numbers $n = 1$ and 2, to *first-principles* calculations for a free standing Na ML [76] in the limit of a large QD ($a \to \infty$). This resulted in $U_0 = 6.21$ eV and $L = 8.57$ au. For further details, we refer the reader to a previous work [61].

3.2. Two-jellium model

The system we consider consists of a 1 ML thick Na QD on top of one complete ML of Na on Cu(111). To mimic the decay of the wavefunctions into the substrate, we introduce a two-jellium model. Within this model, we do not include the electrons of the Cu substrate. Instead, we take a small amount of the electron density from the Na ML, and turn this into a slab of lower density placed below the Na slab, keeping the total charge density constant. The procedure is illustrated in figure 1. For the density of Na, we have used $r_{\mathrm{s}1} = 3.79$ au, calculated from the bulk value of Na, $r_{\mathrm{s}} = 3.93$ au and the observed height of the Na QDs of 5.5 au [19, 20]. The thickness w_2 and density $r_{\mathrm{s}2}$ for the lower density jellium slab representing the Cu substrate give two free parameters. Those are chosen by fitting the band bottoms for the first and second band for 1 and 2 ML to experimental results [16, 66, 71]. This resulted in $r_{\mathrm{s}2} = 6.0$ au and $w_2 = 6.3$ au. The calculations are performed in the context of density functional theory (DFT) [77, 78], using the program package MIKA [79–81] (Multigrid Instead of K-spAce).

In DFT, the many-body Schrödinger equation is replaced by a set of one-electron equations, where the electrons interact via an effective potential, that are solved self-consistently for the electron density $n(\vec{r})$, minimizing the total energy of the system. Due to the cylindrical symmetry, the wavefunction may be separated as

$$\Psi_{m\vec{k}l}(r, z, \phi) = \mathrm{e}^{\mathrm{i}m\phi}U_{m\vec{k}l}(r, z), \tag{5}$$

where m is the azimuthal quantum number and l differentiates between orthogonal states with the same m and $\vec{k}$. Two $\vec{k}$-vectors are used when transferring the finite cylindrical system into a periodic planar system; see below. In axial symmetry ($\vec{r} = (r, z)$) the Kohn–Sham equations take the form

$$-\frac{1}{2}\left(\frac{1}{r}\frac{\partial}{\partial r} + \frac{\partial^2}{\partial r^2} - \frac{m^2}{r^2} + \frac{\partial^2}{\partial z^2} + 2V_{\mathrm{eff}}(\vec{r})\right) \times U_{m\vec{k}l}(\vec{r}) = \varepsilon_{m\vec{k}l}U_{m\vec{k}l}(\vec{r}) \tag{6}$$

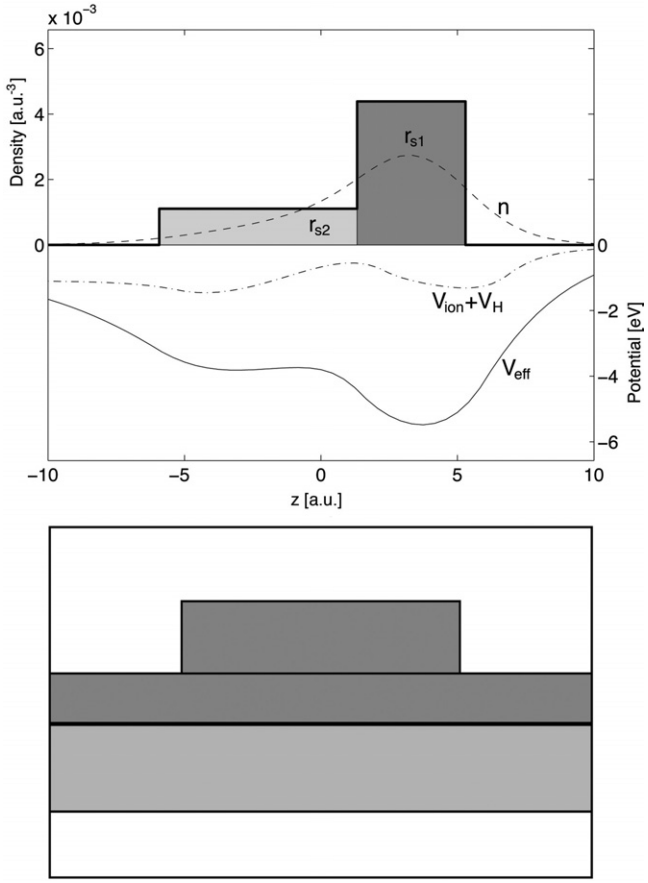

Figure 1. Top: The two-jellium model for 1 ML of Na on Cu(111). The positive background charge is illustrated by the shaded areas. The electron density is indicated by a dashed curve, the effective potential by a solid curve and the electrostatic potential by a dash–dotted curve. Bottom: a schematic figure showing a second ML Na QD dot on Cu(111).

$$n(\vec{r}) = 2\sum_{m\vec{k}l}(2-\delta_{0m})\,f_{m\vec{k}l}|U_{m\vec{k}l}(\vec{r})|^2 \tag{7}$$

$$V_{\rm eff}(\vec{r}) = V_{\rm ion}(\vec{r}) + V_{\rm H}(\vec{r}) + V_{\rm XC}(\vec{r}), \tag{8}$$

$$\left(\frac{1}{r}\frac{\partial}{\partial r} + \frac{\partial^2}{\partial r^2} + \frac{\partial^2}{\partial z^2}\right)V_{\rm H}(\vec{r}) = -4\pi n(\vec{r}). \tag{9}$$

Here, $U_{m\vec{k}l}(\vec{r})$ are the wavefunctions expressed in the (r, z) plane and $\varepsilon_{m\vec{k}l}$ are the one-electron eigenenergies. The electron density in equation (7) is obtained by summing the absolute magnitude of the one-electron wavefunctions squared, weighted by the Fermi–Dirac occupation numbers f_{ml} and multiplied with the degeneracy factor $2(2-\delta_{0m})$. The degeneracy for $m = 0$ is 2, due to the two different spin directions, while for $m \neq 0$ the degeneracy is 4, since $\pm m$ are degenerate.

The effective potential $V_{\rm eff}(\vec{r})$ in equation (8) contains the external potential due to the ionic background $V_{\rm ion}(\vec{r})$, the Hartree potential $V_{\rm H}(\vec{r})$ calculated from the electron density and the exchange–correlation potential $V_{\rm XC}(\vec{r})$ containing the effects of exchange and correlation between electrons. The potential $V_{\rm ion}(\vec{r})$ is treated with the jellium approximation [82, 83],

where the ionic background is replaced by a rigid positive background charge of constant density. The Hartree potential is achieved by solving the Poisson equation (9) for the electron density, and the exchange–correlation potential is treated within the local density approximation (LDA) [84, 85]. The Kohn–Sham equations (6)–(9) are solved self-consistently using the MIKA program package [79–81]. This is a real space code, where the wavefunctions are represented on a three-dimensional (or two-dimensional) point grid, and the equations are discretized using finite differences. The Schrödinger equation is solved using the Rayleigh quotient multigrid method (RQMG) [79], and the Poisson equation (9) is solved with a standard multigrid method [94].

A real space code is perfectly suited for describing finite systems and systems with varying length scales since the grid can be refined locally. However, a uniform planar system cannot be exactly reproduced in the cylindrical symmetry. Instead we adopt a Wigner–Seitz [95] type of approximation scheme, where we imagine the plane exactly filled by hexagons, and approximate these by area-covering circles. We sample the Brillouin zone of the lattice of circles with two $\vec{k}$-points, $\vec{k} = 0$ and $\vec{k}$ at the Brillouin zone boundary. The wavefunctions with $\vec{k} = 0$ are required to have a vanishing radial derivative at the radius of the circle, while the wavefunctions with $\vec{k}$ at the Brillouin zone boundary vanish at the circle boundary. This scheme gives a qualitatively uniform charge distribution, and minimizes the interactions between the object and its periodic images [96, 97]. The convergence of the real space calculation can easily be checked by increasing the number of grid points. This corresponds to changing the energy cut-off in a corresponding plane wave representation. The cell size also plays an important role. For a finite system (like a unsupported QD) there has to be enough vacuum to ensure that the wavefunctions vanish at the boundary, and for a continuous system (as an adsorbed QD on a substrate) the cell has to be large enough to prevent interactions between the QD and its periodic images.

4. Electronic spectrum

When a second ML Na QD is formed on top of the Na overlayer, the electrons within the QD will be quasi-confined to the island structure, and thus show the corresponding quantization. The electron structure calculated for a QD containing 100 electrons with the finite potential well model is presented in the left panel of figure 2, with the energy given with respect to the Fermi energy E_{F}. The energy spectra consist of two bands. The lowest band corresponds to s-type states without any node in the z-direction, while the second band corresponds to unoccupied p states with one node. The two horizontal lines indicate the band edges for a free standing Na ML [76]. The bands show a dispersion with m, where m corresponds to the lateral quantization. Wavefunctions corresponding to states with even m are symmetric in the (r, z) plane with respect to the z-axis, while states with odd m are anti-symmetric. The symmetry of the wavefunction is of great importance when studying properties that depend on the local electronic structure, like the real space electronic structure, local density of states and charge transfer. In the two-jellium model, the band structure will contain two different types of band; see the right panel of figure 2. On one hand there are bands with qualitatively the same dispersion as the free standing quantum dot, corresponding to states with large density within the QD region, but superimposed on these are less dispersed bands corresponding to states with large density in the underlying jellium slabs [62]. These states also show a larger dispersion in k-space.

The density of states (DOS) is defined by

$$D(\epsilon) \equiv \frac{\mathrm{d}N}{\mathrm{d}\epsilon} = \sum_i \delta(\epsilon - E_i), \tag{10}$$

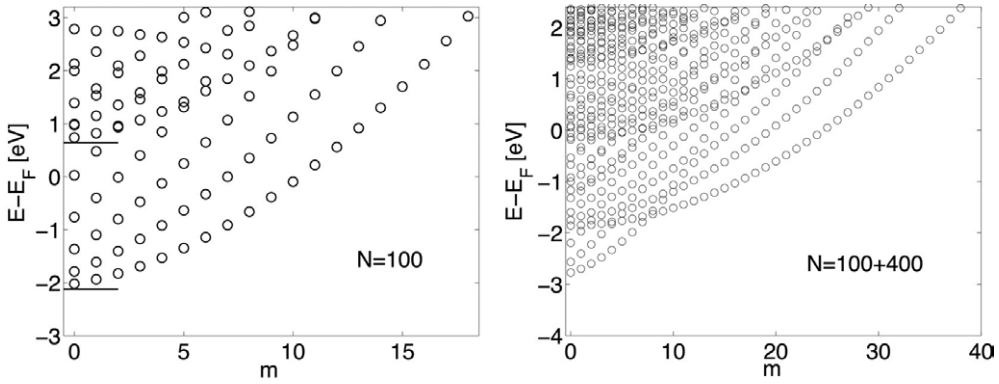

Figure 2. Left: the energy spectrum for a $N = 100$ QD calculated within the finite potential well model. The two horizontal lines indicate the s- and p-band edges for a complete ML [76]. Right: the energy spectrum for a $N = 100$ QD on an $N = 400$ two-jellium slab calculated within the two-jellium model.

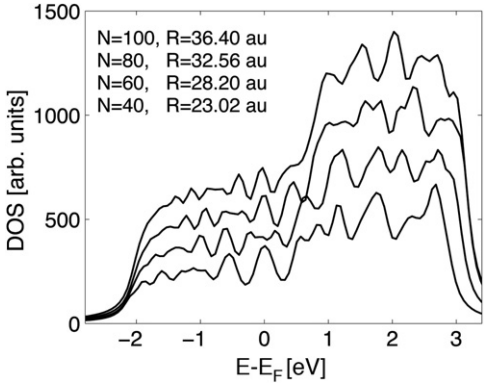

Figure 3. The DOS calculated with the finite potential well model for QDs containing $N = 40$, 60, 80 and 100 electrons. A Lorentzian peak broadening of 0.20 eV has been used.

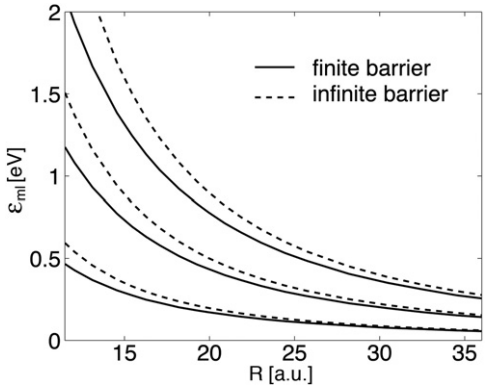

Figure 4. The energy shift as a function of coverage for the three lowest $m = 0$ states, where ε_{ml} is the lateral part of the eigenenergy. The solid curves correspond to the results calculated from the finite potential well model, and the dashed curves correspond to the results from an infinite potential well of the same dimensions.

where N is the number of states. The DOS calculated within the finite potential well model is presented in figure 3. The DOS is approximately constant within each band, which is consistent with the results for a free electron gas in two dimensions [95]. When the radial size of the QD is increased there will be more states in each band. As a result, the onsets of the bands get more pronounced with larger N. There is also a small downshift of the states, which is due to lateral quantum size effects. This is discussed further in section 5.

5. Growth mode

To understand the process of epitaxial growth, monitoring the growth mode of the islands is of great interest. It is important to know whether the islands grow in a two-or three-dimensional mode, and if there are ripening or other effects. One way to get qualitative information about

the growth mode is by measuring the energy downshifts of the overlayer states as a function of coverage by means of PES. Measurements of the energy downshift during the growth of the second ML of Na/Cu(111) were presented by Carlsson *et al* [16, 17]. They observed a downshift of about 30 meV, as the coverage was increased from 1.7 to 2 ML, and interpreted this as a lateral quantum size effect due to 2D island growth.

When the radius of the QD is increased, the energy states will be downshifted. The second term in equation (4) corresponds to the lateral quantization, and is proportional to k_{ml}^2. When the radius of the QD is increased this term will decrease, and by assuming that the number of islands on the surface is constant, the energy downshift as a function of coverage θ can be expressed as

$$-\Delta\varepsilon = \varepsilon_0 \left(1 - \frac{\theta_0}{\theta}\right), \tag{11}$$

the limit of infinite potential barrier [61]. Here, ε is the lateral part of the eigenenergy, and ε_0 is the energy corresponding to the initial coverage θ_0. Comparing the calculated energy downshift with the experimental results provides information on the growth mode, as well as the average island size. By assuming a second ML initial coverage of $\theta_0 = 0.7$, and comparing the results from equation (11) with the observed downshift of 30 meV, we get an average island radius of 25 au. The corresponding downshifts for the infinite barrier calculated by equation (11) and for our finite potential well model are presented in figure 4.

6. Local electronic structure

The physical and chemical properties of a surface are intimately connected to its local electron structure. It plays an important role for surface processes like epitaxial growth [98] and catalysis [99]. The STM is a very useful tool for studying topography and the local electron structure of a surface. The topography is recorded by scanning in either constant current mode or constant height mode, and the LDOS is measured by recording the differential conductance $\mathrm{d}I/\mathrm{d}V$ with applied voltage. At low bias voltage, the differential conductance is proportional to the LDOS [36], defined by

$$\rho(\vec{r}, \epsilon) = \sum_i |\Psi_i(\vec{r})|^2 \delta(\epsilon - E_\mathrm{i}). \tag{12}$$

The LDOS provides the dominant contributions at a given point in space for a certain energy, and by integrating up to the Fermi energy and multiplying with the degeneracy d_i,

$$n(\vec{r}) = d_\mathrm{i} \int_{-\infty}^{E_\mathrm{F}} \rho(\vec{r}, \epsilon) = \sum_i d_\mathrm{i} |\Psi_i(\vec{r})|^2, \tag{13}$$

the electron density is obtained.

Kliewer and Berndt [20] presented a $\mathrm{d}I/\mathrm{d}V$ spectrum for a second ML Na QD on Na/Cu(111) recorded by the STM. In figure 6 we present the LDOS calculated with the two-jellium model for a Na QD of approximately the same size. In our calculations, the QD contains 550 electrons and the underlying slab 2000. The radius of the QD is 85 au, and the cylindrical supercell has a radius of 160 au. Kliewer and Berndt recorded the $\mathrm{d}I/\mathrm{d}V$ slightly off the centre of the island, and to enable a comparison, we calculated the LDOS at a corresponding position. The results are shown in figure 5. The solid curve corresponds to the LDOS calculated 18 au above the centre of the QD, and the dashed curve corresponds to LDOS calculated a distance of 20 au off the centre. The experimental values are indicated by arrows at the top of the figure, where the positions are shifted so that the first experimental peak coincides with our first off-centre peak. At the axis, only the $m = 0$ states contribute while off-centre we will

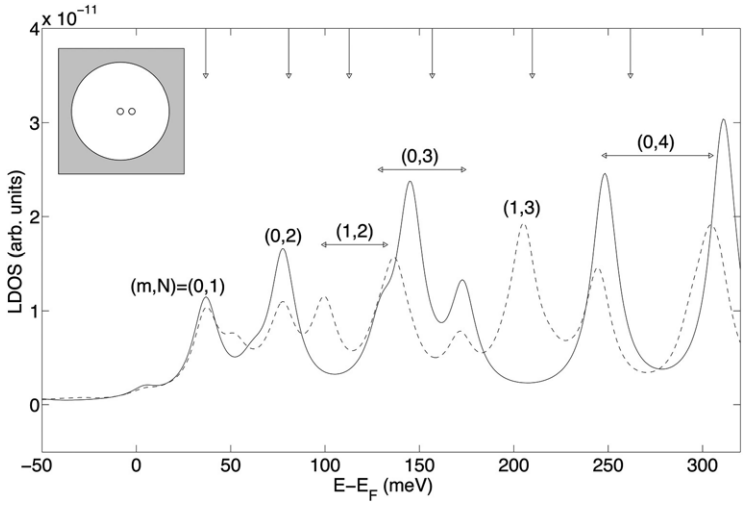

Figure 5. The LDOS corresponding to a $N = 550$ QD on a two-jellium substrate containing 2000 electrons. The LDOS is calculated at a distance of 18 au above the centre of the QD (solid) and at a point 20 au radially from the centre of the QD (dashed); see the inset. A Lorentz broadening of $\Gamma = 8$ meV is used for the peaks. The arrows at the top of the figure indicate the experimentally measured positions for a QD of similar size [20].

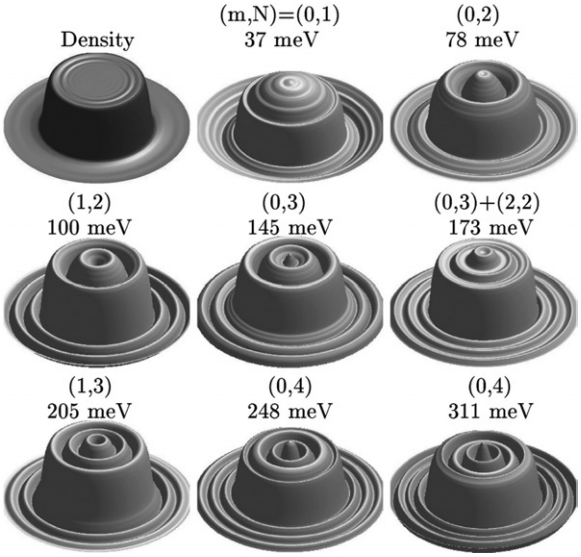

Figure 6. The electron density and the LDOS at energies corresponding to the most pronounced peaks in figure 5. The Lorentzian broadening is $\Gamma = 0.8$ meV.

also have a contribution from states with $m \neq 0$. We have labelled the peaks with m and N, where m is the azimuthal quantum number and $N - 1$ is the number of radial nodes in the QD region. The hybridization of the QD states with the states belonging to the underlying slab causes a splitting of states with binding and anti-binding character. For this reason, some of the peaks in figure 5 belong to the same resonance state. A more thorough discussion on this matter has been presented previously [62].

In figure 6, we present isosurfaces of the LDOS corresponding to the dominant peaks in figure 5, in addition to the electron density. The density is smooth in the interior of the QD, and shows small oscillations towards the edges. The iso-LDOS surfaces show the nodal structure of the individual states, and compare well to experimental results [20].

7. Reactivity

When modelling the reactivity of an adsorbed quantum dot, we choose the system of CO adsorbed on an unsupported Na QD. Our main focus is on studying possible size dependence of the charge transfer between the QD and molecule. We have kept the cylindrical symmetry, requiring the molecule to approach along the symmetry axis with the carbon atom facing downwards. We start by presenting results from a model study based on the Newns–Anderson (NA) model [102, 103] and proceed with a *first-principles* DFT study.

First, we outline the basis of the NA study. The highest occupied molecular orbital (HOMO) for the CO molecule is the filled 5σ orbital which has $m = 0$ character, and the lowest unoccupied molecular orbital (LUMO) is the anti-bonding $2\pi^*$ orbital, which corresponds to the quantum numbers $m = \pm 1$. The 5σ state can host two electrons, while the $2\pi^*$ state can host four, two in each of the $2\pi_x$ and $2\pi_y$ orbitals. The electron affinity for CO is -1.5 eV [100]. The negative sign for the electron affinity indicates that energy is required to impose an extra electron. The CO molecule is represented by $\langle \vec{x}|a\rangle = \langle \vec{x}|2\pi^*\rangle$ and $\langle \bar{x}|k\rangle$ are the QD states. We make the assumption that the coupling matrix elements V_{ak} in the NA model can be described as

$$|V_{ak}| = V_0|\langle a|k\rangle|, \tag{14}$$

where V_0 is a parameter and $\langle a|k\rangle$ the overlap between the $2\pi^*$ orbital and the QD states. The charge transfer is obtained by integrating the projected density of states (PDOS) up to the Fermi level and multiplying with the degeneracy d_a,

$$Q_a = d_a \int_{-\infty}^{E_F} \xi_a(\epsilon)\,\mathrm{d}\epsilon, \tag{15}$$

where the PDOS in the NA model is given by

$$\xi_a(\epsilon) = \frac{1}{\pi}\frac{\Delta(\epsilon)}{(\epsilon - \epsilon_a - \Lambda(\epsilon))^2 + \Delta(\epsilon)^2}, \tag{16}$$

where $\Lambda(\epsilon)$ and $\Delta(\epsilon)$ are the real and imaginary parts of the one-electron self-energy

$$\Delta(\epsilon) = \pi \sum_{\mathrm{k}} |V_{ak}|^2 \delta(\epsilon - \epsilon_{\mathrm{k}}) \tag{17}$$

$$\Lambda(\epsilon) = \frac{P}{\pi}\int \frac{\Delta(\epsilon')}{\epsilon - \epsilon'}\,\mathrm{d}\epsilon'. \tag{18}$$

The QD is described by the finite potential well model, outlined in section 3.1, and the CO molecule by the $2\pi^*$ orbital constructed from normalized linear combinations of Cartesian Gaussians, using the *ab initio* computer code GAMESS [101].

The charge transfer between the unsupported Na QD and the CO molecule as a function of the number of electrons N within the QD is presented in figure 7. It is calculated for a constant height, bond length and interaction parameter [63]. The resulting charge transfer shows a pronounced quantum size dependence, with sharp maxima at $N = 6$, 20, 46 and 76 and minima at $N = 16$, 42 and 72. The peaks correspond to QD sizes, where there exists a filled $m = 1$ state at the Fermi level, indicating that the charge transfer depends critically on the presence of weakly bound QD electrons with the same symmetry as the LUMO of the

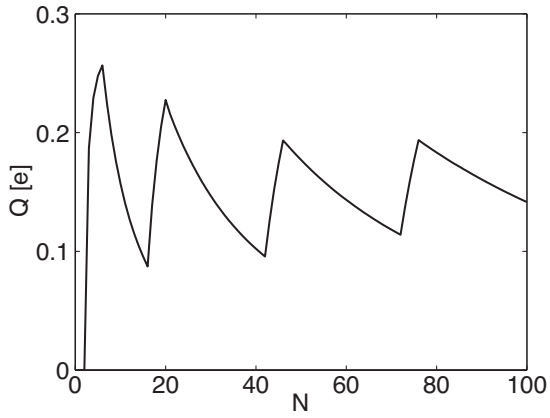

Figure 7. The charge transfer as a function of the number of electrons in the QD, calculated within the NA approximation. We have used the parameters $V_0 = 0.15$, $b_0 = 2.13$ au and $d = 1.11$ au.

CO molecule. The quantum size effects are most pronounced for small QDs, and will vanish for large enough QD radii, since $\langle a|k\rangle$ will obviously decrease with increasing QD size.

The NA model calculation indicates that the charge transfer is quantum size dependent. To investigate this more thoroughly, we have performed a *first-principles* calculation, as outlined in section 3.2, for QDs in the range of $N = 5$–22 electrons [63]. However, to keep a reasonable computational effort, we consider the finite system with an unsupported Na jellium QD. We base this assumption on our previous calculations [62] for the system which indicated that it is the states localized to the QD region that give the predominant contribution to the LDOS above the QD. The CO molecule is represented by pseudopotentials of the Kleinman–Bylander form [104].

The net total energy for the electrons of the combined system, consisting of the CO molecule and the QD, with respect to the values for the corresponding free counterparts, is defined by

$$\Delta E_{\mathrm{Tot}} = E_{\mathrm{Tot}}^{\mathrm{QD+CO}} - (E_{\mathrm{Tot}}^{\mathrm{QD}} + E_{\mathrm{Tot}}^{\mathrm{CO}}). \tag{19}$$

A negative net energy indicates an energetically favourable configuration, while a positive energy indicates that energy is required to obtain the configuration. In figure 8 we present ΔE_{Tot} and the corresponding intermolecular bond length b and bond distance d between the carbon atom and the jellium edge as a function of the number of electrons N in the QD. Each quantity is calculated for the energetically most favourable configuration. We see the same trend as in figure 7. The energetically most favourable size for adsorption is $N = 6$, as for the calculation with the NA model, and the energetically least favourable are the sizes corresponding to $N = 13$–16. For sizes where adsorption is energetically favourable, the CO bond length is increased with respect to the free molecule value ($b_0 = 2.092$ au), indicating that charge transfer to the molecule has taken place.

In figure 9, we present potential energy surfaces (PES) for the two limiting cases. The net total energy is calculated according to equation (19), as a function of molecular bond length b and bond distance d, and displayed on a grid. In the top panel we have the PES corresponding to the $N = 6$ QD with a well-defined minimum at $(b, d) = (2.12, 1.5)$ au, and a net total energy of $\Delta E_{\mathrm{Tot}} = -0.28$ eV. For $N = 16$ on the other hand, the minimum is less pronounced, with $\Delta E_{\mathrm{Tot}} = +0.06$ eV at $(b, d) = (2.10, 4.0)$ au. The bond length is practically the same as for the free molecule, which indicates that the charge transfer to the molecule is small.

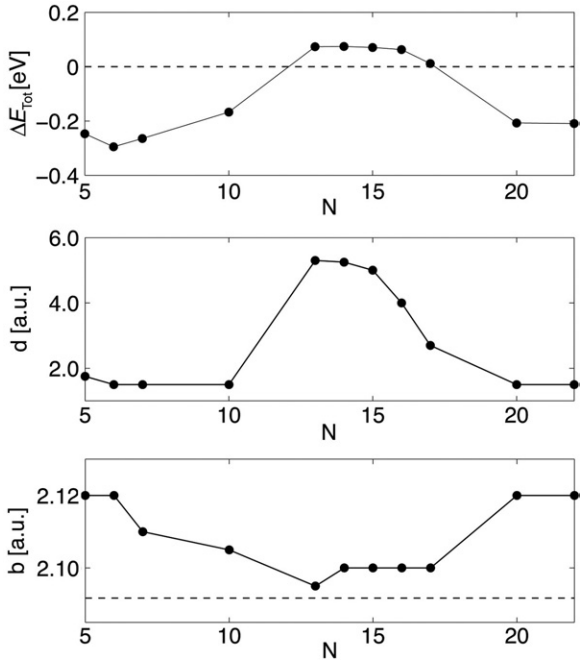

Figure 8. The net total energy (top), the molecule–QD bond distance (middle) and the CO intermolecular bond length (bottom) as a function of the number of electrons within the QD. Each quantity is calculated for a relaxed system, corresponding to the energetically most favourable configuration. The dashed line in the top panel indicates $\Delta E_{\mathrm{Tot}} = 0$, and the dashed line in the bottom panel represents the bond length for the free molecule $b_0 = 2.092$ au.

We calculate the charge transfer according to equation (15), where the PDOS is defined by

$$\xi_a(\epsilon) = \sum_i |\langle i|a\rangle|^2 \delta(\epsilon - \epsilon_i). \tag{20}$$

Here, $|i\rangle$ are the self-consistent one-electron states of the combined CO and QD system and $|a\rangle$ is either the CO HOMO (5σ) or LUMO ($2\pi^*$) orbital. For $N = 16$ the charge transfer was $Q_{2\pi^*} = 0.5e$, while for $N = 6$, $Q_{2\pi^*} = 1.6e$. Thus, we see a considerably larger charge transfer for $N = 6$ as compared with $N = 16$, as indicated already by the PES in figure 9. In figures 10 and 11 we present the PDOS for the $N = 6$ and 16 QDs, calculated for $d = 2.0$, 6.0 and 10.0 au. In addition, we show the wavefunctions corresponding to the most pronounced peaks in the $2\pi^*$ PDOS, calculated for $d = 10.0$ au and the energetically most favourable bond distance for each size. The change in electron density for the CO molecule when adsorbed on the $N = 6$ QD is presented in figure 12. We observe an increased density with $2\pi^*$ symmetry, and a decrease in electron density with 5σ symmetry, as expected from the Blyholder model [105].

The origin of why the charge transfer is considerably larger for $N = 6$ than for $N = 16$ is understood by studying the electronic spectra for each case; see figures 13(a) and (b). The $2\pi^*$ molecular orbital is formed by a linear combination of states with angular momenta +1 and −1. As a consequence, only QD states with $|m| = 1$ will contribute to the charge transfer. For $N = 6$ we have a completely filled $m = 1$ state just below the Fermi level, while for $N = 16$, this $m = 1$ state has been downshifted in energy, and the next $m = 1$ state is still above E_{F}. From this we conclude that the presence of occupied electron states, with the same symmetry

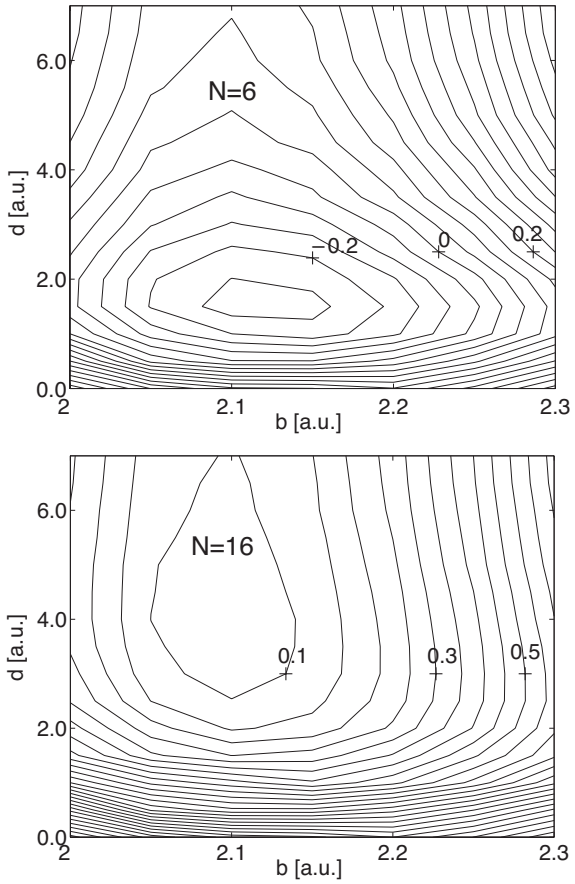

Figure 9. The PES for $N = 6$ (top) and $N = 16$ (bottom) QDs. The molecular bond length b and the distance d between the centre of the carbon atom and the upper jellium edge are given in au. The net total energy is given in eV, and the energy difference between two successive levels is 0.05 eV.

as the LUMO for the adsorbing molecule, close to the Fermi level is crucial for an enhanced charge transfer.

In addition to the radius, the height also presents a size parameter within our model. Increasing the radius of the QD allows states with higher m quantization to fit and induces more states in each band, while increasing the height of the QD downshifts the energy states and compresses the bands, since states with higher n quantum number will show a larger downshift. In figure 13(c) we show the energy spectrum for a 2 ML thick QD with the same radius as the $N = 16$ QD in figure 13(b). The increased height results in an energy spectrum with two $m = 1$ states practically at the same energy, just below the Fermi level. The resulting charge transfer to the $2\pi^*$ orbital is in this case $0.93e$ at $d = 4.0$ au, almost twice the amount for the 1 ML $N = 16$ QD. Thus, by controlling the radius and height of the QD, it is in principle possible to tune the energy spectrum to promote a certain property.

We have illustrated that the size parameters influence the electron spectrum, and thus the local electronic properties of the adsorbed QD. These properties are in turn determined by the adsorbate, underlying substrate and the growth process itself. The average island size and the growth mode are often delicate, and depend on temperature, evaporation rate, pressure,

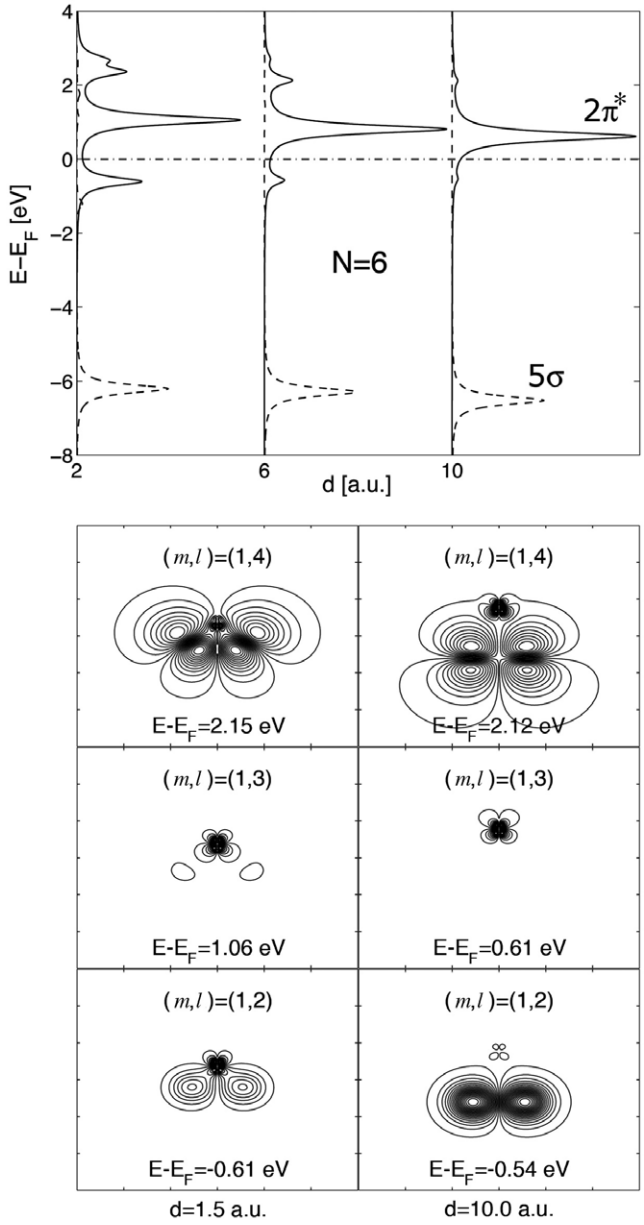

Figure 10. Top: the PDOS corresponding to the 5σ and $2\pi^*$ states, calculated for the $N = 6$ QD at bond distances d. Bottom: the wavefunctions for $m = 1$ states with indices l, corresponding to $d = 1.5$ and 10.0 au. The bond length is kept constant at $b = 2.12$ au.

presence of impurities etc. In addition, coordination and interface effects have proved to be important, especially for the catalytic properties of adsorbed clusters and nanoparticles.

8. Summary and conclusion

During the last decade experimental and theoretical studies of adsorbed nanoscale metallic clusters have revealed several features of great interest for applications in a new field—

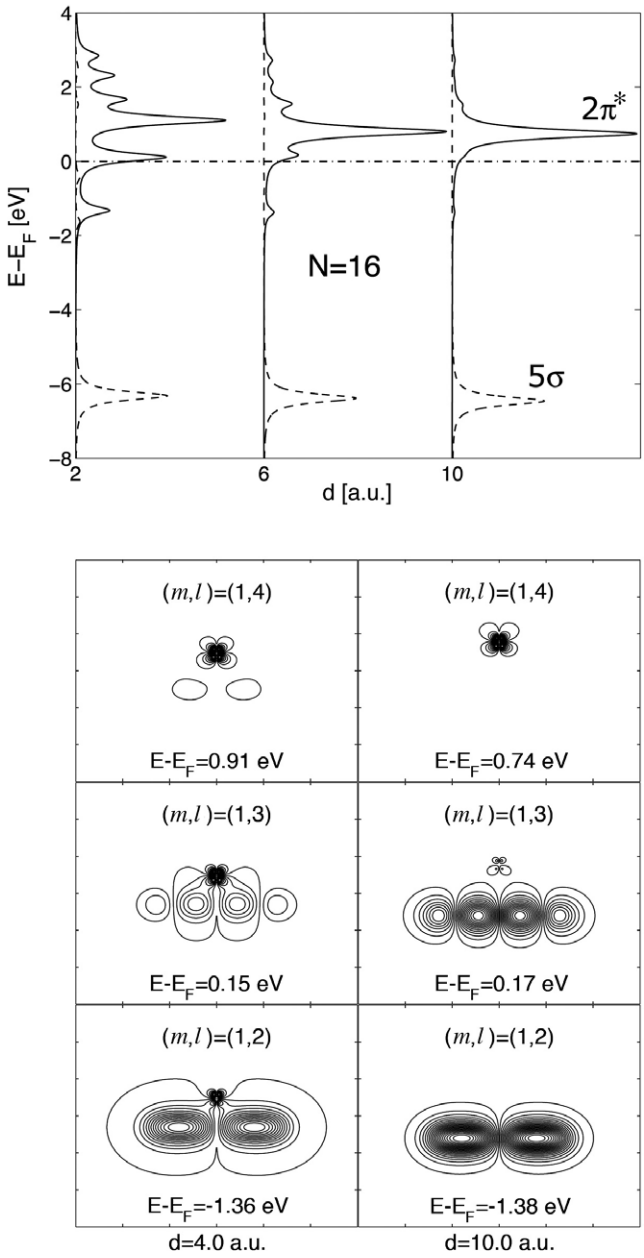

Figure 11. Top: the PDOS corresponding to the 5σ and $2\pi^*$ states, calculated for the $N = 16$ QD at bond distances d. Bottom: the wavefunctions for $m = 1$ states with indices l, corresponding to $d = 4.0$ and 10.0 au. The bond length is kept constant at $b = 2.10$ au.

nanocatalysis. In this paper we have summarized some of these achievements. In addition, we have in more detail presented our own recent theoretical investigations of adsorbed metallic quantum dots. We have calculated the energy shifts, electron density and local density of states and compared our results to experimental results from STM and PES. In addition, we have modelled CO reactivity on an unsupported Na QD, by calculating the charge transfer with the

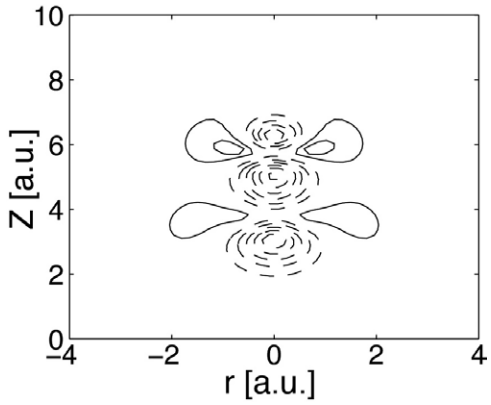

Figure 12. The change in electron density up on CO adsorption on a $N = 6$ QD. The solid curves indicate an increased electron density, while dashed curves indicate a decrease. The molecule is positioned along the z-axis, with the C atom at 3.69 and O at 5.81 au. The QD jellium edge is located at $z = -0.31$ au.

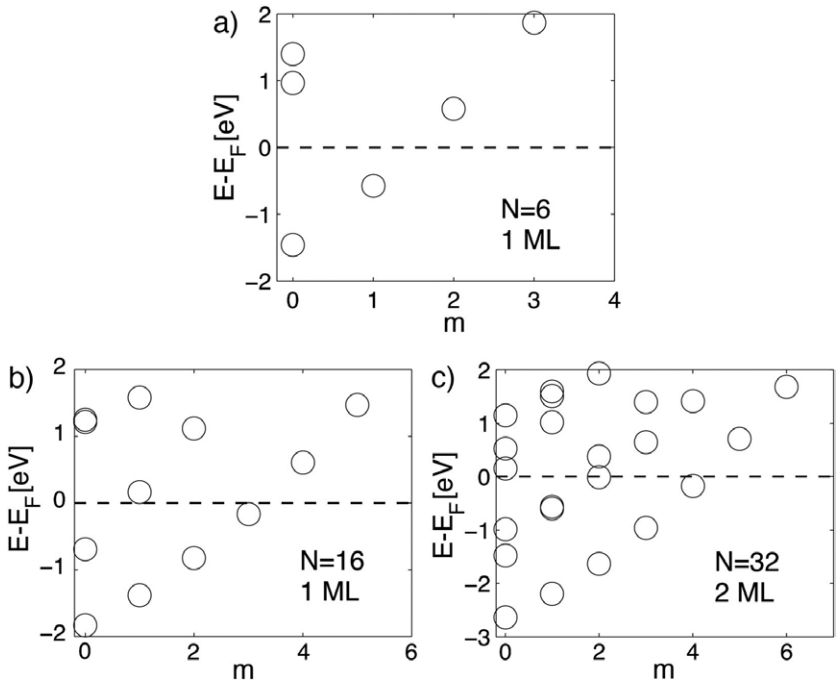

Figure 13. The energy eigenstates for (a) the $N = 6$ QD, (b) the $N = 16$ QD and (c) a 2 ML thick QD with the same radius as for $N = 16$.

Newns–Anderson model and from *first principles*. We observed a pronounced size dependence in the charge transfer, which could be explained in terms of the presence of weakly bound QD electrons with the same symmetry as the LUMO of the reacting molecule. In conclusion, we indeed find that by changing the size parameters of the adsorbed quantum dot, it is possible to control the reactivity.

Acknowledgments

The authors would like to acknowledge Dr T Torsti and Professors M J Puska and R M Nieminen for collaboration during the work with the two-jellium model. T Petersson is acknowledged for collaboration in the Newns–Anderson model calculation. CSC and Helsinki University of Technology (HUT) are acknowledged for the generous computer resources and for providing access to the MIKA program package.

References

[1] Crommie M F, Lutz C P and Eigler D M 1993 *Science* **262** 218
[2] Avouris P and Lyo I-W 1994 *Science* **264** 942
[3] Schmid G and Corain B 2003 *Eur. J. Inorg. Chem.* **2003** 3081
[4] Gardea-Torresday J L, Parson J G, Gomez E, Peralta-Videa J, Troiani H E, Santiago P and Yacaman M J 2002 *Nano Lett. (Communication)* **2** 397
[5] Haruta M, Kobayashi T, Sano H and Yamada N 1987 *Chem. Lett.* **2** 405
[6] Haruta M 1997 *Catal. Today* **36** 153
[7] Grisel R J H and Nieuwenhuys B E 2001 *J. Catal.* **199** 48
[8] Valden M, Lai X and Goodman D W 1998 *Science* **281** 1647
[9] Choudary T V and Goodman D W 2002 *Top. Catal.* **21** 25
[10] Lüth H 1993 *Surfaces and Interfaces of Solids* (Berlin: Springer)
[11] Heller E J 1984 *Phys. Rev. Lett.* **53** 1515
[12] Heller E J, Crommie M F, Lutz C P and Eigler D M 1994 *Nature* **369** 464
[13] Roder H, Hahn E, Brune H, Bucher J-P and Kern K 1993 *Nature* **366** 141
[14] Li J, Schneider W-D, Berndt R and Crampin S 1998 *Phys. Rev. Lett.* **80** 3332
[15] Li J, Schneider W-D, Crampin S and Berndt R 1999 *Surf. Sci.* **422** 95
[16] Carlsson A, Lindgren S-Å, Svensson C and Walldén L 1994 *Phys. Rev.* B **50** 8926
[17] Carlsson A, Hellsing B, Lindgren S-Å and Walldén L 1997 *Phys. Rev.* B **56** 1593
[18] Kliewer J and Berndt R 2001 *Surf. Sci.* **477** 250
[19] Kliewer J and Berndt R 2001 *Phys. Rev.* B **65** 035412
[20] Kliewer J and Berndt R 2001 *Appl. Phys.* A **72** S155
[21] Venables J A 1994 *Surf. Sci.* **299/300** 798
[22] Venables J A 2000 *Introduction to Surface Thin Film Process* (London: Cambridge University Press)
[23] Suekane O, Hasegawa S, Takata M, Okui T and Nakashima H 2002 *Mater. Sci. Eng.* B **88** 158
[24] Nakata Y, Mukai K, Sugawara M, Ohtsubo K, Ishikawa H and Yokoyama N 2000 *J. Cryst. Growth* **208** 93
[25] Madhukar A, Xie Q, Chen P and Konkar A 1994 *Appl. Phys. Lett.* **64** 2727
[26] Solomon G S, Trezza J A and Harris J S 1995 *Appl. Phys. Lett.* **66** 991
[27] Solomon G S, Trezza J A and Harris J S 1995 *Appl. Phys. Lett.* **66** 3161
[28] Suzuki T, Temko Y and Jacobi K 2003 *Phys. Rev.* B **67** 045315
[29] Fisher B, Brune H, Barth J V, Fricke A and Kern K 1999 *Phys. Rev. Lett.* **82** 1732
[30] Michely T, Hohage M, Bott M and Comsa G 1993 *Phys. Rev. Lett.* **70** 3943
[31] Kalff M, Comsa G and Michely T 1998 *Phys. Rev. Lett.* **81** 1255
[32] Brune H 1998 *Surf. Sci. Rep.* **31** 121
[33] Brune H, Giovannini M, Bromann K and Kern K 1998 *Nature* **394** 451
[34] Binnig G, Rohrer H, Gerber Ch and Weibel E 1982 *Phys. Rev. Lett.* **49** 57
[35] Binnig G and Rohrer H 1986 *IBM J. Res. Dev.* **30** 355
[36] Tersoff J and Hamann D R 1985 *Phys. Rev.* B **31** 805
[37] Besenbacher F 1996 *Rep. Prog. Phys.* **59** 1737
[38] Ruan L, Besenbacher F, Stensgaard I and Lægsgaard E 1992 *Phys. Rev. Lett.* **69** 3523
[39] Bennet P A and von Kanel H 1999 *J. Phys. D: Appl. Phys.* **32** R71
[40] Kliewer J, Berndt R, Chulkov E V, Silkin V M, Echenique P M and Crampin S 2000 *Science* **288** 1399
[41] Dahl S, Logadottir A, Egeberg R C, Larsen J H, Chorkendorff I, Törnqvist E and Nørskov J K 1999 *Phys. Rev. Lett.* **83** 1814
[42] Heiz U, Sanchez A, Abbet S and Schneider W-D 2000 *Chem. Phys.* **262** 189
[43] Heiz U and Schneider W-D 2000 *J. Phys. D: Appl. Phys.* **33** R85
[44] Holmgren L, Andersson M and Rosén A 1995 *Surf. Sci.* **331–333** 231

[45] Valden V, Pak S, Lai X and Goodman D W 1998 *Catal. Lett.* **56** 7
[46] Sanchez A, Abbet S, Heiz U, Schneider W-D, Häkkinen H, Barnett R N and Landman U 1999 *J. Phys. Chem.* A **103** 9573
[47] Choudhary T V and Goodman D W 2002 *Top. Catal.* **21** 25
[48] Lai X and Goodman D W 2000 *J. Mol. Catal.* A **162** 33
[49] Griesel R J H, Kooyman P J and Nieuwenhuys B E 2000 *J. Catal.* **191** 430
[50] Salama T M, Ohnishi R and Ichikawa M 1996 *J. Chem. Soc. Faraday Trans.* **92** 301
[51] Hayashi T, Tanaka K and Haruta M 1998 *J. Catal.* **178** 566
[52] Lemire C, Meyer R, Shaikhutdinov S and Freund H J 2004 *Angew. Chem. Int. Edn Engl.* **43** 118
[53] Boccuzzi F, Chiorino A and Manzoli M 2001 *Mater. Sci. Eng.* C **15** 215
[54] Haruta M 2002 *CATTECH* **6** 102
[55] Pietron J J, Stroud R M and Rolison D R 2002 *Nano Lett.* **2** 545
[56] Mavrikakis M, Stoltze P and Nørskov J K 2000 *Catal. Lett.* **64** 101
[57] Lopez N and Nørskov J K 2002 *J. Am. Chem. Soc.* **124** 11262
[58] Molina L M and Hammer B 2003 *Phys. Rev. Lett.* **90** 206102
[59] Molina L M and Hammer B 2004 *Phys. Rev.* B **69** 155424
[60] Molina L M, Rasmussen M D and Hammer B 2004 *J. Chem. Phys.* **120** 7673
[61] Lindberg V and Hellsing B 2002 *Surf. Sci.* **506** 297
[62] Torsti T, Lindberg V, Puska M J and Hellsing B 2002 *Phys. Rev.* B **66** 235420
[63] Lindberg V, Petersson T and Hellsing B 2005 submitted
[64] Diehl R and McGrath R 1996 *Surf. Sci. Rep.* **23** 43
[65] Lindgren S Å and Walldeén L 1987 *Phys. Rev. Lett.* **59** 3003
[66] Lindgren S Å and Walldén L 1988 *Phys. Rev.* B **38** 3060
[67] Hamawi A, Lindgren S Å and Walldén L 1991 *Phys. Scr.* T **39** 339
[68] Tang D, McIlroy D, Shi X, Su C and Heskett D 1991 *Surf. Sci. Lett.* **255** L497
[69] Gartland P O and Slagsvold B J 1975 *Phys. Rev.* B **12** 4047
[70] Heimann P, Neddermeyer H and Roloff H F 1977 *J. Phys. C: Solid State Phys.* **10** L17
[71] Fischer N, Schuppler S, Fischer R, Fauster Th and Steinmann W 1991 *Phys. Rev.* B **43** R14722
[72] Fischer N, Schuppler S, Fischer R, Fauster Th and Steinmann W 1994 *Surf. Sci.* **314** 89
[73] Dudde R, Johansson L S O and Reihl B 1991 *Phys. Rev.* B **44** 1198
[74] Carlsson J M and Hellsing B 2000 *Phys. Rev.* B **61** 13973
[75] Hellsing B, Carlsson J M, Walldén L and Lindgren S Å 2000 *Phys. Rev.* B **61** 2343
[76] Wimmer E 1983 *J. Phys. F: Met. Phys.* **13** 2313
[77] Hohenberg P and Kohn W 1964 *Phys. Rev.* **136** B864
[78] Kohn W and Sham L J 1965 *Phys. Rev.* **140** A1133
[79] Heiskanen M, Torsti T, Puska M J and Nieminen R M 2001 *Phys. Rev.* B **63** 245106
[80] Torsti T, Heiskanen M, Puska M J and Nieminen R M 2003 *Int. J. Quantum Chem.* **91** 171
[81] Torsti T, Lindberg V, Makkonen I, Ogando E, Räsänen E, Saarikoski H, Puska M J and Nieminen R M 2004 Ψ_k *Newsletter* **65** 105
[82] Lang N D 1983 *Theory of the Inhomogeneous Electron Gas* ed S Lundqvist and N H March (New York: Plenum)
[83] Lang N D 1994 *Surf. Sci.* **299/300** 284
[84] Ceperley D M and Alder B J 1980 *Phys. Rev. Lett.* **45** 566
[85] Perdew J P and Zunger A 1981 *Phys. Rev.* B **23** 5048
[86] Schulte F K 1976 *Surf. Sci.* **55** 427
[87] Manninen M, Nieminen R M, Hautojärvi P and Arponen J 1975 *Phys. Rev.* B **12** 4012
[88] de Heer W A 1993 *Rev. Mod. Phys.* **65** 611
[89] Zabala N, Puska M J and Nieminen R M 1998 *Phys. Rev. Lett.* **80** 3336
[90] Zabala N, Puska M J and Nieminen R M 1999 *Phys. Rev.* B **59** 12652
[91] Puska M J, Ogando E and Nieminen R M 2001 *Phys. Rev.* B **64** 033401
[92] Havu P, Torsti T, Puska M J and Nieminen R M 2002 *Phys. Rev.* B **66** 075401
[93] Ogando E, Torsti T, Puska M J and Zabala N 2003 *Phys. Rev.* B **67** 075417
[94] Brandt A 1977 *Math. Comput.* **31** 333
[95] Kittel C 1996 *Introduction to Solid State Physics* 7th edn (New York: Wiley)
[96] Makov G, Shah R and Payne M C 1996 *Phys. Rev.* B **53** 15513
[97] Korhonen T, Puska M J and Nieminen R M 1996 *Phys. Rev.* B **54** 15016
[98] Memmel N and Bertel E 1995 *Phys. Rev. Lett.* **75** 485
[99] Bertel E, Roos P and Lehmann J 1995 *Phys. Rev.* B **52** R14384

[100] Huber K P and Herzberg G 1979 *Molecular Spectra and Molecular Structure* vol 4 *Constants of Diatomic Molecules* (New York: Van Nostrand-Reinhold)
[101] Schmidt M W, Baldridge K K, Boatz J A, Elbert S T, Gordon M S, Jensen J H, Koseki S, Matsunaga N, Nguyen K A, Su S J, Windus T L, Dupuis M and Montgomery J A 1993 *J. Comput. Chem.* **14** 1347
[102] Anderson P W 1961 *Phys. Rev.* **124** 41
[103] Newns D M 1969 *Phys. Rev.* **178** 1123
[104] Kleinman L and Bylander D M 1982 *Phys. Rev. Lett.* **48** 1425
[105] Blyholder G 1964 *J. Phys. Chem.* **68** 2772